Self-Assembly and Chain-Folding in Hybrid Coil−Coil−Cube Triblock Oligomers of Polyethylene-*b*-Poly(ethylene oxide)-*b*-Polyhedral Oligomeric Silsesquioxane

Jianjun Miao,[†] Li Cui,[†] Henry P. Lau,[†,§] Patrick T. Mather,[‡] and Lei Zhu*[,†]

Polymer Program, Institute of Materials Science and Department of Chemical, Materials and Biomolecular Engineering, University of Connecticut, Storrs, Connecticut 06269-3136, and Department of Macromolecular Science and Engineering, Case Western Reserve University, Cleveland, Ohio 44106

Received March 31, 2007; Revised Manuscript Received May 10, 2007

ABSTRACT: Self-assembly and chain-folding in well-defined oligomeric polyethylene-*block*-poly(ethylene oxide)-*block*-polyhedral oligomeric silsesquioxane (PE-*b*-PEO-*b*-POSS) triblock molecules were studied by small-angle X-ray scattering (SAXS), wide-angle X-ray diffraction (WAXD), and transmission electron microscopy (TEM). The triblock oligomers were synthesized by attaching two kinds of functional POSS molecules, namely, isocyanatopropyldimethylsilylisobutyl-POSS (Ib−POSS) and isocyanatopropyldimethylsilylcyclopentyl-POSS (Cp−POSS), to a hydroxyl-terminated PE-*b*-PEO-OH diblock oligomer (denoted as $E_{39}EO_{23}$) via urethane reactions. In these triblock oligomers, both PE and POSS were crystalline, whereas PEO became amorphous due to tethering of its both ends to other two blocks. In the crystalline state, PE chains tilted 32° from the lamellar normal, and both Ib−POSS and Cp−POSS molecules stacked into four-layer (ABCA) lamellar crystals, having the same trigonal ($R\bar{3}m$) symmetry as in pure POSS crystals. Because the cross-sectional area for a PE chain in the PE crystals (0.216 nm^2/chain) at the interface was much smaller than that for a POSS molecule in POSS crystals (1.136 nm^2/molecule), the self-assembly and PE chain-folding were substantially affected by the sequence of PE and POSS crystallization when crystallizing from the melt. For example, PE crystallization induced the POSS crystallization in the bulk $E_{39}EO_{23}$−Ib−POSS, and thus extended-chain PE crystals were observed. The grains of crystalline lamellae again were small with often highly curved lamellar crystals. This could also be attributed to the unbalanced interfacial areas for POSS and PE blocks (the interfacial area ratio being 2.6 for interdigitated PE crystals, i.e., two PE chains per POSS molecule). For the $E_{39}EO_{23}$−Cp−POSS triblock oligomer, POSS molecules crystallized before PE crystallization, forming a well-defined lamellar structure. The preexisting POSS crystals confined the PE crystallization, and thus almost once-folded PE crystals were obtained. Because the interfacial area ratio between POSS and PE blocks decreased to 1.3, the crystalline lamellae were straight and their grains were relatively large. On the basis of this study, we conclude that confinement effect plays an important role on chain-folding of crystalline block oligomers, which in turn determines the unbalanced cross-sectional areas between chemically different blocks and finally dictates their final crystalline morphology.

Introduction

Because of a balance between the free energy penalties from chain-folding of the crystalline block and chain-stretching of the amorphous block, chain-folding has been predicted to be under equilibrium conditions, rather than being kinetically controlled processes for high molecular weight semicrystalline diblock copolymers. The crystalline lamellar thickness (L) scaled as $L \sim N_t N_a^{\alpha}$, where N_t and N_a are the degrees of polymerization for the entire diblock and the amorphous block, respectively. Here, α is a constant, e.g., $-1/3$ reported in ref 1, $-5/12$ in ref 2, and $-6/11$ in ref 3. Experimental results reasonably agreed with theoretical predictions for high molecular weight block copolymers.[4−8] Unlike high molecular weight semicrystalline block copolymers, crystalline block oligomers exhibited extended, fractionally folded, and integrally folded chain crystals. Therefore, the crystalline lamellar thickness for oligomeric block copolymers does not obey the above predicted rules for high molecular weight block copolymers, where the equilibrium crystalline lamellar thickness changes continuously with the molecular weight of the crystallizable block.

Experimentally, equilibrium integral chain-folding was observed to take place at a lower threshold molecular weight for oligomeric block copolymers, when compared with the crystallizable oligomeric homologues.[9−15] This was due to the unbalanced cross-sectional areas between the crystalline and amorphous blocks at the crystal−melt interfaces, in addition to the need of filling spaces at approximately constant densities as in the bulk. Besides equilibrium integral chain-folding, metastable multiply folded (including nonintegrally folded) structures were induced by rapid crystallization of the crystalline block oligomers.[13,15,16] Annealing these metastable and multiply folded crystals at elevated temperatures could thicken the crystalline lamellae.[14] In a recent study on an amphiphilic starlike molecule with an aliphatic core and four hydrophilic PEO arms (molecular weight = 2000 g/mol), the difference between the interfacial areas of the core and four PEO chains induced once-folded chain PEO crystals, and transitions from once-folded to extended-chain PEO crystals took place via fractionally folded crystals.[17] If the molecular weight of the crystallizable oligoblock further decreases, extended-chain crystals are preferred, regardless of the molecular size of the other block. As a result, unbalanced surface stresses will accumulate during the lateral growth of a lamellar crystal, and finally lamellar crystals have to break from time to time, resulting in small grains on the order of one to a few hundred

* Corresponding author: e-mail lei.zhu@uconn.edu; Tel 860-486-8708.
[†] University of Connecticut.
[‡] Case Western Reserve University.
[§] Current address: Department of Chemical and Biomolecular Engineering, Cornell University, Ithaca, NY 14853.

10.1021/ma070770w CCC: $37.00 © 2007 American Chemical Society
Published on Web 06/28/2007

nanometers. In other words, chain-folding can be bypassed by forming small crystalline grains with extended-chain crystals for semicrystalline block oligomers. This was exactly observed in a recent study on a polyethylene-*b*-poly(ethylene oxide)-*b*-triphenylene (PE-*b*-PEO-*b*-P5T) triblock oligomer.[18] However, it is still unclear under what conditions a crystalline block oligomer will adopt multiply folded chains with balanced interfacial areas (in this case the grain size of crystalline lamellae should be relatively large) or extended chains with unbalanced interfacial areas (in this case the grain size of crystalline lamellae should be small).

In this study, we successfully attached an oligomeric PE-*b*-PEO diblock copolymer to an incompressible cubic molecule, i.e., polyhedral oligomeric silsesquioxane (POSS). Note that there are only a few studies of crystallizable oligomers attached to incompressible spherical molecules, such as C_{60} and POSS,[19,20] and no chain-folding was discussed in those systems. In the PE-*b*-PEO-*b*-POSS triblock oligomers, the cross-sectional areas for a PE chain and a POSS molecule are 0.216 and 1.136 nm^2, respectively. The self-assembly behavior of the triblock oligomer and the PE chain-folding are found to be dictated by the difference in the interfacial areas between a PE chain and a POSS molecule and the sequence of PE and POSS crystallization as well. If PE crystallized prior to POSS when crystallizing from the melt (i.e., unconfined crystallization), extended-chain PE crystals are preferred. The grains of crystalline lamellae are relatively small (only ∼100−300 nm) because the interfacial area ratio between a POSS molecule and a PE chain is as high as 2.6 (note that PE chains are interdigitated and thus one POSS molecule corresponds to two PE chains at the interface). In addition, curved lamellar crystals are observed as a result of unbalanced surface stresses. On the other hand, when the POSS crystallized prior to PE when crystallizing from the melt, PE crystallization will be confined between preexisting POSS lamellar crystals. Once-folded chain PE crystals are obtained, and the interfacial area ratio between a POSS molecule and a PE chain decreases to 1.3. As a consequence, straight crystalline lamellae with relatively large grain sizes (at least >500 nm) are observed.

Experimental Section

Materials. Toluene was freshly distilled over calcium hydride before use. Hydroxyl-terminated PE-*b*-PEO-OH was purchased from Aldrich. Size-exclusion chromatography (SEC) and differential scanning calorimetry (DSC) results indicated that it had a broad molecular weight distribution with a contamination of short alkanes and PEO homopolymers. A low molecular weight fraction with a narrow molecular weight distribution was obtained by fractionation and purification using toluene as the solvent, as described in a previous report.[21] The molecular weight of each block was determined by end-group analysis using proton nuclear magnetic resonance (^{1}H NMR) to be 1080 g/mol in the PE block and 998 g/mol in the PEO block. The molecular weigh distribution of the sample was 1.16 as determined by SEC, using polystyrene as standards and tetrahydrofuran (THF) as the mobile phase. Therefore, this diblock copolymer is denoted as $E_{39}EO_{23}$. Isocyanatopropyldimethylsilylcyclopentyl-POSS (Cp−POSS) was purchased from Aldrich, and isocyanatopropyldimethylsilylisobutyl-POSS (Ib−POSS) was purchased from Hybrid Plastics (Hattiesburg, MS). Both POSS samples were used without further purification.

Synthesis of $E_{39}EO_{23}$−POSS Triblock Oligomers. The chemical structures of two $E_{39}EO_{23}$−POSS triblock oligomers are shown in Scheme 1, and they were synthesized by reactions of isocyanate POSS with hydroxyl-terminated $E_{39}EO_{23}$-OH, using a slightly modified method from the literature.[20,22,23] Typically, 434 mg (0.29 mmol) of $E_{39}EO_{23}$ was dispersed in 35 mL of dry toluene and transferred to two-neck flask under a dried N_2 atmosphere. The

Scheme 1. Chemical Structures of $E_{39}PEO_{23}$−Cp−POSS and $E_{39}PEO_{23}$−Ib−POSS

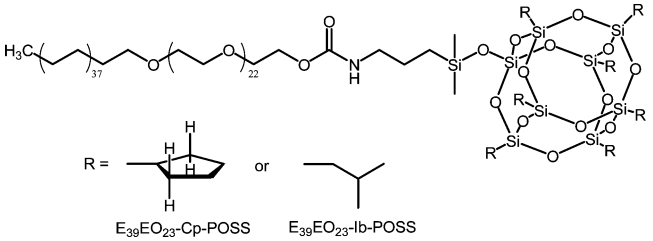

solution with a PE crystal suspension was heated up to 90 °C and then became clear. 0.36 mmol of POSS (350 mg of Ib-POSS or 381 mg of Cp-POSS) dissolved in 9 mL of dry toluene with three drops of the catalyst, dibutyltin dilaurate, was added dropwise to the reaction flask over a period of 30 min. The reaction mixture was stirred at 90 °C for overnight. The reaction mixture was concentrated and precipitated in excessive *n*-hexane. The unreacted POSS and impurity were removed by repeated precipitation in *n*-hexane. The precipitate was then redissolved in THF and precipitated in excessive methanol three times to partially remove unreacted $E_{39}EO_{23}$. After drying the samples in a vacuum oven for 24 h to remove residue methanol, column chromatography on silica gel using an eluent of hexane:THF = 1:3 (v/v) was performed to obtain pure $E_{39}EO_{23}$−POSS triblock oligomers. Finally, the yields for both $E_{39}EO_{23}$−Cp−POSS and $E_{39}EO_{23}$−Ib−POSS were about 60%. The purity of both samples was confirmed by SEC and ^{1}H NMR (see Supporting Information). Quantitative ^{1}H NMR data are summarized below.

^{1}H NMR for $E_{39}EO_{23}$−Cp−POSS: δ ($CDCl_3$) 0.13 (s, 6H, Si−C*H*$_3$), 0.58 [t, 2H, Si−C*H*$_2$−(CH$_2$)$_2$NH−], 0.89 [t, 3H, C*H*$_3$−(CH$_2$)$_n$−], 0.98 (t, 7H, Si−C*H*), 1.26 [s, 150H, −(C*H*$_2$)$_n$−], 1.50−1.76 [m, 56H, cyclopentyl −(C*H*$_2$)$_4$−], 3.15 (t, 2H C*H*$_2$−NH−COO), 3.45 [t, 2H, −(CH$_2$)$_n$−C*H*$_2$−(OCH$_2$CH$_2$)$_m$−], 3.66 [s, 89H, −(OC*H*$_2$C*H*$_2$)$_m$−], 4.21 [t, −OCH$_2$C*H*$_2$−OCONH−].

^{1}H NMR for $E_{39}EO_{23}$−Ib−POSS: δ ($CDCl_3$) 0.12 (s, 6H, Si−C*H*$_3$), 0.57 [t, 2H, Si−C*H*$_2$−(CH$_2$)$_2$NH−], 0.61 [t, 7H, Si−C*H*$_2$−CH(CH$_3$)$_2$], 0.89 [t, 3H, C*H*$_3$−(CH$_2$)$_n$−], 0.97 [s, 42H, Si−CH$_2$−CH(C*H*$_3$)$_2$], 1.26[s, 150H, −(C*H*$_2$)$_n$−], 1.62[m, 2H, −CONHCH$_2$C*H*$_2$CH$_2$Si(CH$_3$)$_2$O−], 1.86 [m, 7H, Si−CH$_2$−C*H*(CH$_3$)$_2$], 3.15 (t, 2H C*H*$_2$−NH−COO), 3.45 [t, 2H, −(CH$_2$)$_n$−C*H*$_2$−(OCH$_2$CH$_2$)$_m$−], 3.66 [s, 89H, −(OC*H*$_2$C*H*$_2$)$_m$−], 4.22 [t, −OCH$_2$C*H*$_2$−OCONH−].

Instrumentation and Characterization. ^{1}H NMR spectra were recorded on a Bruker spectrometer (500 MHz, DMX 500). Differential scanning calorimetry (DSC) experiments were carried out on a TA DSC-Q100 instrument. An indium standard was used for both temperature and enthalpy calibration. Approximately 1 mg sample was used for the DSC study, and the scanning rate was 5 °C/min. SEC was performed on a Viscotek GPCmax with quadruple detectors. THF was used as the solvent, and polystyrene standards were used for calibration.

Two-dimensional (2D) simultaneous SAXS and WAXD experiments were performed at the synchrotron X-ray beamline X27C at National Synchrotron Light Source, Brookhaven National Laboratory. The wavelength of X-ray was 0.1371 nm. The scattering angle was calibrated using silver behenate with the primary reflection peak at the scattering vector $q = (4\pi \sin\theta)/\lambda = 1.076\ nm^{-1}$, where θ is the half-scattering angle and λ is the wavelength. Fuji imaging plates were used as detectors for both SAXS and WAXD experiments, and digital images were obtained using a Fuji BAS-2500 scanner. The typical data requisition time was 1 min. An Instec HCS410 hot stage equipped with a liquid nitrogen cooling accessory was used in temperature-dependent X-ray experiments. One-dimensional (1D) SAXS and WAXD curves were obtained by integration of the corresponding 2D SAXS and WAXD patterns. The azimuthal scans were performed on 2D WAXD patterns with the zero-angle starting from the meridian and scanning counterclockwise.

TEM experiments were performed on a Philips EM300 at an accelerating voltage of 80 kV. Thin sections with thicknesses ∼75−

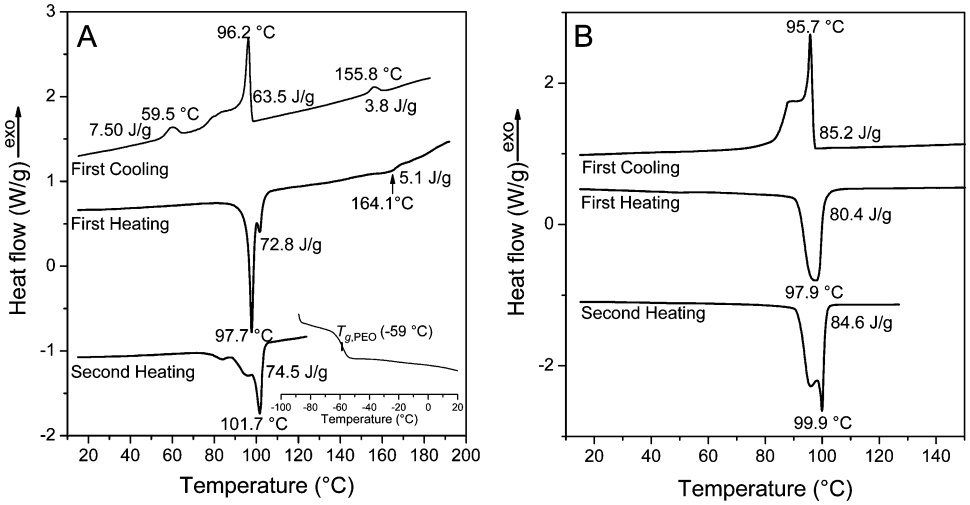

Figure 1. DSC curves of the first heating, first cooling, and second heating processes for (A) $E_{39}EO_{23}$−Cp−POSS and (B) $E_{39}EO_{23}$−Ib−POSS. The scanning rate is 5 °C/min.

100 nm were obtained using a Leica Ultracut UCT microtome with a diamond knife at −10 °C. Thin section samples were collected onto 400 mesh TEM grids, freeze-dried, and stained in RuO_4 vapor at room temperature for 20 min.[21]

Results and Discussion

Thermal Behaviors Studied by DSC. The thermal behaviors of starting materials, Cp−POSS, Ib−POSS, and $E_{39}EO_{23}$, were studied by DSC (see Supporting Information). Cp−POSS had a melting temperature (T_m) at 357.3 °C with a heat of fusion of ca. 43.8 J/g (or 46.4 kJ/mol). Ib−POSS had a T_m at 136.6 °C with a heat of fusion of 20.4 J/g (or 19.9 kJ/mol). We expect that the dramatic difference in the melting points of Ib−POSS and Cp−POSS will affect the self-assembly of the $E_{39}EO_{23}$−POSS triblock molecules. For the $E_{39}EO_{23}$, the T_ms of PE and PEO crystals were observed at 101.3 °C (126.8 J/g) and 26.7 °C (36.5 J/g), respectively. Since the heats of fusion for E_{39} and EO_{23} oligomers were approximately 299.9 and 150.4 J/g,[21] the crystallinities of PE and PEO were calculated to be about 81 and 51 wt %, respectively.

Thermal behaviors of $E_{39}EO_{23}$−Cp−POSS and $E_{39}EO_{23}$−Ib−POSS triblock oligomers during the first heating, first cooling, and second heating processes are shown in parts A and B of Figure 1, respectively. For both samples, the EO_{23} block became completely amorphous after one free end being attached to a POSS molecule. For example, in the $E_{39}EO_{23}$−Cp−POSS only the PEO glass transition temperature (T_g) was seen at −59 °C in the inset of Figure 1A. Both original samples were cast from 5 wt % THF solutions at room temperature. Since THF was a good solvent for the PEO block and POSS, but a poor solvent for the PE block at room temperature, the PE blocks crystallized first in concentrated THF solutions when the solution became concentrated enough. We speculate that the POSS molecules crystallized after the solvent was almost fully evaporated.

During the first heating for the $E_{39}EO_{23}$−Cp−POSS, a sharp T_m for the PE block was seen at 97.7 °C with a higher temperature shoulder at 101.5 °C. The total heat of fusion was 72.8 J/g. The T_m for the Cp−POSS crystal was seen at 164.1 °C with a heat of fusion of 5.1 J/g. Obviously, when attaching Cp−POSS to the $E_{39}EO_{23}$, the T_m of Cp−POSS crystals drastically dropped from 357.3 to 164.1 °C. After normalization to the weight percentage of Cp−POSS in the $E_{39}EO_{23}$−Cp−POSS (i.e., 33.8 wt %), the Cp−POSS heat of fusion was 15.1 J/g, much lower than that (43.8 J/g) for the neat Cp−POSS. During cooling, Cp−POSS crystallization peak (T_c) was seen at 155.8 °C with a heat of crystallization being 3.8 J/g. The PE crystallization had a sharp T_c at 96.2 °C with a very broad tail at lower temperatures. The total heat of transition for both the sharp and broad peaks was 63.5 J/g. Interestingly, another T_c for PE crystallization was seen at 59.5 °C with a heat of transition of 7.5 J/g. Judging from such a low T_c for the PE crystallization, we attributed it to homogeneously nucleated crystallization.[24−26] Apparently, the crystallization at higher temperatures could be attributed to the heterogeneously nucleated PE crystallization. Both heterogeneous and homogeneous nucleation-induced polymer crystallization processes have also been observed in semicrystalline block copolymers.[27−29] Finally, during the second heating, multiple PE crystal melting peaks were observed with a major peak T_m at 101.7 °C, which is about 4 °C higher than that for the $E_{39}EO_{23}$−Cp−POSS cast from the THF solution (see the first heating). Since the heat of fusion for this broad peak was 74.5 J/g, the PE crystallinity could be calculated to be 73.5 wt %, slightly lower than that for the neat $E_{39}EO_{23}$.

During the first heating of $E_{39}EO_{23}$−Ib−POSS, a single and relatively broad T_m was seen at 97.9 °C with a heat of fusion of 80.4 J/g (Figure 1B). During the cooling, a major and sharp T_c was seen at 95.7 °C, together with a broad shoulder at 88.7 °C. During the second heating, double PE crystal melting peaks were observed with a major T_m at 99.9 °C and a broad lower temperature shoulder at 96.0 °C. The total heat of fusion was 84.6 J/g. No T_m was observed around 136.6 °C for the Ib−POSS crystals. This is understandable because the T_m of Ib−POSS should decrease after attaching Ib−POSS to the $E_{39}EO_{23}$, similar to the case in $E_{39}EO_{23}$−Cp−POSS. On the basis of a simultaneous SAXS and WAXD study (see results later), Ib−POSS crystallized almost coincidentally with the PE block in the $E_{39}EO_{23}$−Ib−POSS. To calculate PE crystallinity, the heat of fusion for Ib−POSS should be deducted from the total heat of fusion. Because the heats of fusion for Ib−POSS and PE in $E_{39}EO_{23}$ were 20.4 and 244 J/g, the PE crystal heat of fusion was calculated to be 78.3 J/g. The PE crystallinity was thus calculated to be 81.6 wt %, which had been normalized to the Ib−POSS weight fraction of 32.0 wt %.

Crystal Structure and Orientation Studied by 2D SAXS and WAXD. To obtain the information on crystal structure and crystal orientation, the $E_{39}EO_{23}$−Cp−POSS sample was shear-oriented at 98−102 °C between two aluminum plates before

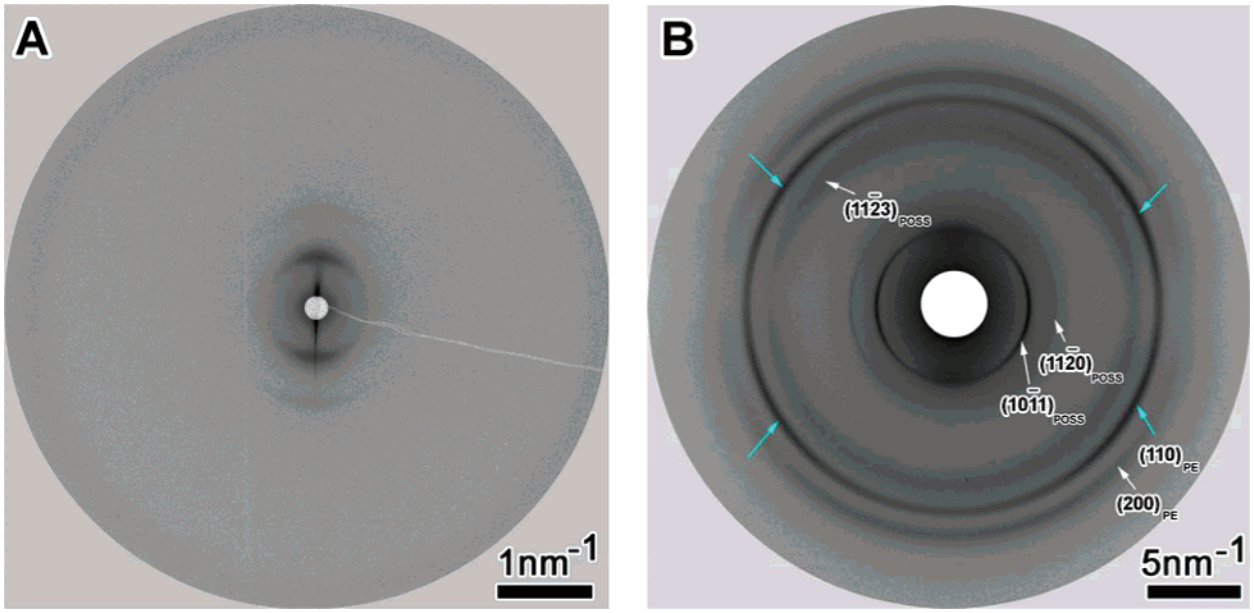

Figure 2. Two-dimensional (2D) (A) SAXS and (B) WAXD patterns for the shear-oriented $E_{39}EO_{23}$−Cp−POSS triblock oligomer. The film was aligned in the horizontal direction. The Miller indices for POSS (*hkil*) and PE (*hkl*) crystals are shown in the 2D WAXD pattern in (B).

quenching to room temperature. The X-ray beam was along the shear direction, and the film was aligned horizontally. Figure 2A shows a 2D SAXS pattern for the shear-oriented $E_{39}EO_{23}$−Cp−POSS sample, and the corresponding 2D WAXD pattern is shown in Figure 2B. Judging from the breadth of the reflection arcs in Figure 2B, the degree of crystal orientation was poor. We speculate that the volume fraction of Cp−POSS crystals is too small (ca. 27 vol %) to allow perfect alignment along the shear direction, although there is enough mechanical contrast between the molten PE and crystalline POSS. In the 2D SAXS pattern, up to 2 orders of lamellar reflections with an overall *d*-spacing of 11.57 nm are seen in the meridian, consistent with the horizontal orientation of a lamellar structure comprising of crystalline PE, amorphous PEO, and crystalline Cp−POSS layers.

Information on PE crystal orientation could be obtained from the 2D WAXD pattern in Figure 2B, where the PE (110) and (200) reflections at $q = 15.1$ and 16.7 nm^{-1}, respectively, are seen in the quadrants. From the azimuthal scan results (see the cyan arrows in Figure 2B for reflection maxima and Supporting Information), we calculated that the PE chains tilted at an angle of 32° from the lamellar normal. Broad Cp−POSS crystal reflection arcs, $(10\bar{1}1)$ and $(11\bar{2}0)$, are centered on the equator in the 2D WAXD pattern in Figure 2B, and overlapped $(11\bar{2}3)$/$(30\bar{3}0)$ reflections do not show any preferred orientation. To determine the Cp−POSS and Ib−POSS crystal structures, 1D WAXD results for $E_{39}EO_{23}$−Cp−POSS and $E_{39}EO_{23}$−Ib−POSS are compared with pure Cp−POSS and Ib−POSS X-ray diffraction profiles (see Figure S5 in Supporting Information). Because major crystal reflections from the POSS crystals in $E_{39}EO_{23}$−Cp−POSS and $E_{39}EO_{23}$−Ib−POSS were exactly the same as those in pure Cp−POSS and Ib−POSS, the POSS crystals in the triblock oligomers should have the same crystalline structure as pure POSS crystals. TEM electron diffraction (ED) was also attempted to elucidate the structure of POSS crystals; however, single crystals of Cp−POSS could not be successfully obtained due to the interference between PE and POSS crystallization.

Pure POSS molecules with eight symmetric alkyl substituents crystallized into layers of hexagonally packed cubes (or spheres), which further stacked into an ABC sequence, not an AB sequence. Because it was not a close packing which is a face-centered cubic or fcc structure, the crystal system belonged to a trigonal (rhombohedral) structure with a space group of $R\bar{3}m$.[30−32] When one alkyl side group was replaced by a functional group, the asymmetric POSS molecules still fitted into the ABC-stacked rhombohedral structure with slight variations in the unit cell dimensions.[33,34] When POSS molecules were attached to polymers, X-ray diffraction results showed that the POSS crystals in the hybrid polymers displayed the same major crystal reflections as those from pure POSS crystals.[35−38] Lamellar morphology with alternating bilayer POSS crystals and polymer lamellae was inferred for these polymers. In a recently study on the supramolecular self-assembly of a disk−cube dyad molecule, lamellar POSS crystals with an four-layer ABCA stacking sequence was determined by 2D WAXD experiments and computer simulation of the X-ray diffraction.[39]

Because each POSS molecule is attached to an $E_{39}EO_{23}$ diblock oligomer, the stacking number of hexagonally packed POSS layers cannot exceed four. On the basis of our previous report (especially the computer simulation result of X-ray diffraction from a slab containing an ABCA four-layer lamella with spherical molecules),[39] a possible structure is described as the following; each POSS crystalline lamella must have a thickness of at least one *c*-axis dimension, i.e., four layers of hexagonally packed POSS molecules stacking into an ABCA sequence. Using the 1D WAXD results in Figure S5, the POSS crystal unit cell dimensions can be tentatively determined as $a = 1.62$ nm, $c = 1.72$ nm, and $\gamma = 120°$, and it is almost the same for both pure POSS and $E_{39}EO_{23}$−POSS samples. In this study, we used four-parameter hexagonal indices (*hkil*) to describe a rhombohedral structure, where $i = -(h + k)$. However, instead of using the [*uvtw*] indices to represent the lattice directions, we adopted the [*UVW*] system, where $U = 2h + k = u - t$, $V = h + 2k = v - t$, and $W = 1.5l(a/c)^2 = w$.[39,40]

As reported in ref 39, the Cp−POSS diffraction pattern in Figure 2B can be explained reasonably well using a model of horizontally aligned POSS lamellar crystals with an ABCA four-layer stacking sequence, as shown in Figure 3B,C. For details one should refer to the Supporting Information. On the basis of the above experimental results, a plausible molecular model is

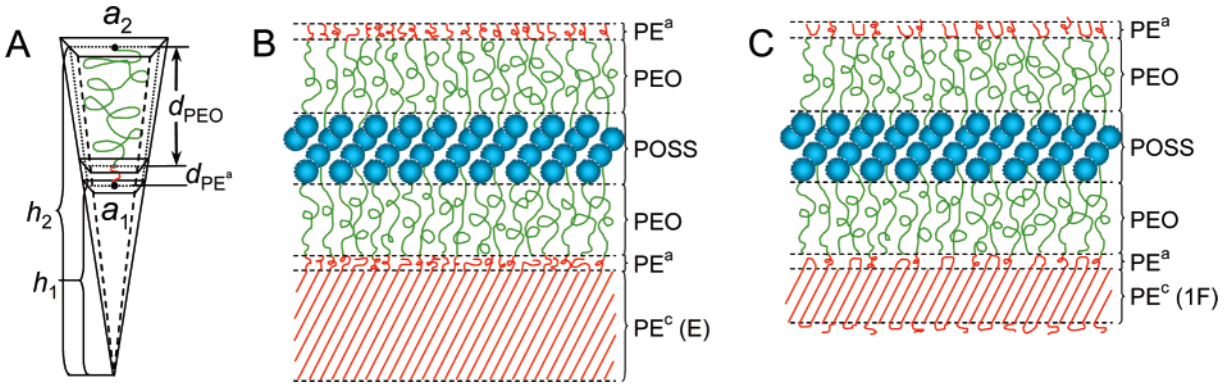

Figure 3. (A) Schematic representation of the pyramidal frustum for the amorphous part of the $E_{39}EO_{23}$ chain in $E_{39}EO_{23}$−POSS samples. (B) Schematic representation of one lamellar repeat for the $E_{39}EO_{23}$−POSS with extended-chain PE crystals. (C) Schematic representation of one lamellar repeat for the $E_{39}EO_{23}$−POSS with once-folded chain PE crystals.

shown in Figure 3B,C, where an amorphous PEO layer is sandwiched between a four-layer ABCA POSS lamella and a PE crystal with PE *c*-axes tilted 32° from the lamellar normal.

Predicting Lamellar Thicknesses in $E_{39}EO_{23}$−POSS with Extended and Once-Folded PE Chains. As we mentioned earlier in the Introduction, chain-folding in crystalline block copolymers is predicted under equilibrium conditions (rather than a kinetically controlled process) due to a balance between the free energy penalties from chain-folding of the crystalline block and chain-stretching of the amorphous block.[1−3] For oligomeric block copolymers, equilibrium integral chain-folding was observed, which occurred at a lower threshold molecular weight when compared to the oligomeric homologues.[9−15] This was a direct result of the difference in cross-sectional areas of the two blocks at the interface, coupled with a need of space-filling at constant bulk densities for different blocks.

Different cross-sectional areas of the PE chain and POSS also happened in the $E_{39}EO_{23}$−POSS oligomers. Figure 3A shows a schematic representation of different cross-sectional areas for a PE chain (area a_1 at the interface between crystalline and amorphous PE) and a POSS molecule (area a_2 at the interface of amorphous PEO and crystalline POSS) in $E_{39}EO_{23}$−POSS. These cross-sectional areas would form a pyramidal frustum, comprising amorphous PE and PEO blocks. When the PE chains adopted the extended-chain conformation, they were interdigitated and tilted 32° from the layer normal (see Figure 3B). Each PE chain cross-sectional area can be calculated to be $a_1 = 0.5a_{PE}b_{PE}/\cos 32° = 0.216$ nm^2 on the basis of PE unit cell dimensions ($a_{PE} = 0.7418$ nm and $b_{PE} = 0.4946$ nm).[21] From our SAXS results (see below) of the overall lamellar thickness of ~14.5 nm, the possibility of a double-layer crystalline structure with extended PE chains (overall lamellar thickness would be ~20.5 nm) can be eliminated. In Figure 3B, there are two POSS molecules in the *c*-projection of one hexagonal unit cell in a POSS crystal. Each POSS molecule, therefore, has a cross-sectional area of $a_2 = (\sqrt{3}/4)a_{POSS}^2 = 1.136$ nm^2. Because the PE chains are interdigitated, the ratio of the POSS and PE interfacial areas is $a_2/2a_1 = 2.6$. We speculate that such a difference in the cross-sectional areas will accumulate mechanical stresses during the lateral growth of a crystal and affect the self-assembly and crystallization behaviors of $E_{39}EO_{23}$−POSS triblock oligomers.

Assuming the density of amorphous PE and PEO in the diblock copolymer is the same as those for bulk samples (0.825 and 1.061 g/cm^3 for amorphous PE and PEO, respectively),[21] the volume of the amorphous part of PE-*b*-PEO can be evaluated as

$$V = V_{PE^a} + V_{PEO} = \frac{M_{PE^a}}{\rho_{PE^a}} + \frac{M_{PEO}}{\rho_{PEO}} \quad (1)$$

where M_{PE^a} is the molecular weight of the amorphous part of a PE block (calculated based on PE crystallinity) and $M_{PEO,a}$ is the molecular weight of the PEO block. Because the pyramidal frustum is the difference of two pyramids (the heights of these pyramids are h_1 and h_2), the ratio of h_1/h_2 is

$$h_1/h_2 = \sqrt{a_1/a_2} \quad (2)$$

and the volume of the pyramid frustum is

$$V = \frac{1}{3}(a_2h_2 - a_1h_1) \quad (3)$$

From eqs 2 and 3, the total thickness of the amorphous PE and PEO layers is $d = h_2 - h_1$. Assuming the amorphous PE and PEO separated into two layers with thicknesses being d_{PE^a} and d_{PEO}, respectively, and the interfacial area between amorphous PE and PEO being a_{PE-PEO}, the following relationships also hold:

$$h_1/(h_1 + d_{PE^a}) = \sqrt{a_1/a_{PE-PEO}} \quad (4)$$

and the volume of the amorphous PE frustum can be calculated as

$$V_{PE^a} = \frac{1}{3}[a_{PE-PEO}(h_2 + d_{PE^a}) - a_1h_1] \quad (5)$$

Using eqs 3 and 4, the d_{PE^a} can be calculated:

$$d_{PE^a} = \sqrt[3]{\frac{h_1^2}{a_1}(3V_{PE^a} + a_1h)_1} - h_1 \quad (6)$$

The amorphous PEO layer thickness is thus $d_{PEO} = d - d_{PE^a}$. Crystalline PE layer thickness is calculated on the basis of the PE crystallinity, x^c:

$$d_{PE^c} = \frac{M_{PE}x^c}{M_0} c_{PE} \cos 32° \quad (7)$$

where M_{PE} is the PE block molecular weight, M_0 is the molecular weight of an ethylene repeat unit (28 g/mol), c_{PE} is the *c*-axis dimension (0.2546 nm), and the chain tilting angle is 32°. Then the POSS layer thickness is roughly

$$d_{POSS} = 2R_{POSS} + c_{POSS} \quad (8)$$

where R_{POSS} is the radius of a POSS molecule, which is about 0.5 nm,[39] and the c_{POSS} is 1.72 nm. The POSS layer thickness is thus 2.72 nm.

If the PE chain is once-folded (see Figure 3C), the cross-sectional area per PE chain doubles, i.e., $a_1 = 0.432$ nm^2. Assuming PE chains are still interdigitated, the ratio between the POSS and PE cross-sectional areas decreases to $a_2/2a_1 = 1.3$. This will, to a large extent, release the unbalanced interface stresses and facilitate PE crystal lateral growth. The calculated layer thicknesses for extended and once-folded $E_{39}EO_{23}$−POSS samples are shown in Table 1. These data will be compared with experimental results in the following discussion.

Extended-Chain PE Crystals in $E_{39}EO_{23}$−POSS Grown from Solution. To achieve unconfined crystallization for the PE blocks, both $E_{39}EO_{23}$−Cp−POSS and $E_{39}EO_{23}$−Ib−POSS samples were cast from THF solutions at ambient temperature. PE blocks crystallized before the POSS crystallization because THF is a good solvent for POSS but a poor solvent for PE at room temperature. Figure 4 shows SAXS profiles for solution-cast $E_{39}EO_{23}$−Cp−POSS and $E_{39}EO_{23}$−Ib−POSS samples, whose overall lamellar thicknesses are 14.5 and 14.9 nm, respectively. Compared with calculated overall lamellar thicknesses in Table 1, extended-chain PE crystals were obtained for both samples cast from THF. The morphology of $E_{39}EO_{23}$−Cp−POSS and $E_{39}EO_{23}$−Ib−POSS samples with extended-chain PE crystals was studied by TEM, and the results are shown in parts A and B of Figure 5, respectively. In the enlarged TEM insets, one can clearly see that white/thick PE layers are sandwiched by two dark/thin PEO layers. Meanwhile, between two adjacent dark PEO layers, another white/thin POSS layer is seen. These results are consistent with our previous RuO_4-staining results on crystalline PE, amorphous PEO, and crystalline POSS.[21,39] From the inset TEM image in Figure 5A, each layer thickness for PE, PEO, and POSS can be obtained by scanning the intensity of brightness across the lamellae (data not shown). This TEM analysis method has been reported before.[17,41] The experimental thicknesses for solution-grown $E_{39}EO_{23}$−Cp−POSS are listed in Table 1 for comparison with the calculated thicknesses. As one can see, the experimental results based on TEM analysis matched reasonably well to the calculated layer thicknesses. Judging from the PE layer thickness of 7.3 ± 0.9 nm (large errors originate from the small lamellar grain sizes), which is close to total PE layer thickness (i.e., $2PE^a + PE^c = 8.25$ nm), the amorphous PE should not be stained by RuO_4. This is consistent with our previous report that hydrogenated polybutadiene cannot be stained by RuO_4.[42] Under low magnifications, the grain sizes of these lamellae are small for both samples, in the range of 100−300 nm. Similarly, small grain size was also observed in a PE-*b*-PEO-*b*-P5T triblock oligomer.[18] We attribute the small grain sizes to the unbalanced interfacial areas between a PE block and a POSS molecule (i.e., $a_2/2a_1 = 2.6$), when PE chains adopted the extended-chain conformation. When the PE crystals grow along the lateral direction, unfavorable stress can accumulate to destabilize further growth, and thus the PE crystalline grains have to be small.

Extended-Chain PE Crystals Grown from the Melt in $E_{39}EO_{23}$−Ib−POSS. From the DSC results in Figure 1B, we speculate that both PE and POSS should melt and crystallize tandemly. Figure 6 shows the heating SAXS and WAXD profiles with a small temperature interval of 2 °C for $E_{39}EO_{23}$−Ib−POSS. At 88 °C, sharp first-, second-, and third-order lamellar reflections coexisted with a broad correlation-hole scattering in the SAXS profile in Figure 6A, suggesting a partial melting of the sample. In the WAXD profiles, with a gradual increase in temperature, the intensities of POSS ($10\bar{1}1$) and PE (110) reflections decreased simultaneously, and finally both POSS and PE crystals melted after being heated above 98 °C. Two amorphous halos centered at 5.4 and 14.2 nm^{-1} were seen in the WAXD profile for $E_{39}EO_{23}$−Ib−POSS at 100 °C. The halo at 5.4 nm^{-1} (d-spacing = 1.16 nm) was attributed to the average distance between cubic POSS molecules, whose diameters were around 1.0 nm. The halo at 14.2 nm^{-1} (d-spacing = 0.442 nm) was explained as the average distance between PEO and PE chains. In the SAXS profile at 100 °C, a broad correlation-hole scattering was seen at 0.98 nm^{-1} (d-spacing = 6.4 nm), which represented the average distance among the PE-rich, PEO-rich, and POSS-rich microdomains in a density fluctuation-induced disordered phase.[43,44]

Figure 7 shows the cooling SAXS and WAXD profiles with a small temperature interval of 2 °C for $E_{39}EO_{23}$−Ib−POSS. During a cooling process from the melt at 100 °C, POSS ($10\bar{1}1$) and PE (110) reflections started to appear simultaneously at 96 °C in the WAXD profile in Figure 7B, together with up to 3 orders of lamellar reflections in the SAXS profile in Figure 7A. Decreasing the temperature just further increased the crystallinities of both POSS and PE.

On the basis of these experimental results, we concluded that POSS and PE melted and crystallized within a very narrow temperature range (<2 °C) around 100 °C. A similar phenomenon was also observed for the PE-*b*-PEO-*b*-P5T triblock oligomer, where the isotropization of the discotic triphenylene took place coincidently with the PE crystal melting.[18] Taking into account of the melting temperatures for the pure Ib−POSS and the PE crystals in $E_{39}EO_{23}$ being 136.6 and 101.3 °C, respectively, we speculated that PE melting (or crystallization) triggered the melting (or crystallization) of POSS. In other words, immediately after PE crystals melted, molten PE blocks served as an additional solvent to dissolve POSS crystals upon heating to above its melting point. Upon cooling, after the PE crystallization, the volume fraction of POSS in the melt suddenly increased and thus induced subsequent POSS crystallization. In this sense, the PE crystallization was unconfined, and this was believed to be responsible for the formation of extended-chain PE crystals.

The morphology of melt-grown $E_{39}EO_{23}$−Ib−POSS with extended-chain PE crystals was studied by TEM, and the images are shown in Figure 8. In a low-magnification view in Figure 8A, the crystalline lamellae are often curved with relatively small grain sizes on the order of one to a couple hundred nanometers. The inset TEM image shows a high-magnification view of a grain having straight lamellae. From this TEM image, each layer thickness for PE, PEO, and POSS can again be obtained by TEM image analysis when comparing the brightness scan profile with the TEM image in Figure 9A. The results are listed in Table 1 for melt-grown $E_{39}EO_{23}$−Ib−POSS. As one can see, the experimental results based on TEM analysis matched very well to the calculated layer thicknesses. Again, judging from the PE layer thickness of 8.4 ± 0.2 nm, which is almost the same as the total PE layer thickness (i.e., $2PE^a + PE^c = 8.32$ nm), the amorphous PE should not be stained by RuO_4. On the basis of these results, extended-chain PE crystals were indeed obtained when $E_{39}EO_{23}$−Ib−POSS was grown from the melt. The relatively small grains can also be attributed to the unbalanced cross-sectional area ratio of $a_2/2a_1 = 2.6$ for the extended-chain PE conformation in the crystalline lamellae, as

Table 1. Calculated and Experimental (Determined by Both SAXS and TEM) Thicknesses for $E_{39}EO_{23}$−POSS Samples with Extended and Once-Folded Chain PE Crystals

	with extended-chain PE crystal		with once-folded chain PE crystal	
lamellar thicknesses	calculated (nm)	experimental (nm)	calculated (nm)	experimental (nm)
		$E_{39}EO_{23}$−Cp−POSS (crystallinity = 73.5 wt %)		
POSS	2.72	2.7 ± 0.2[a]	2.72	2.4 ± 0.2[b]
PEO	1.76	2.2 ± 0.1[a]	1.51	1.9 ± 0.1[b]
PE^{am}	1.09 } 8.25[d]	7.3 ± 0.9[a]	0.65 } 4.34[d]	4.6 ± 0.3[b]
PE^{cr}	6.07 }		3.04 }	
total[c]	14.48	14.5[a]	10.08	10.8[b]
		$E_{39}EO_{23}$−Ib−POSS (crystallinity = 81.6 wt %)		
POSS	2.72	2.6 ± 0.1[b]	2.72	
PEO	1.81	1.8 ± 0.2[b]	1.52	
PE^{am}	0.81 } 8.32[d]	8.4 ± 0.2[b]	0.47	
PE^{cr}	6.70 }		3.35	
total[c]	14.68	14.6[b] or 14.9[a]	10.05	

[a] Crystallized and cast from THF solution. [b] Crystallized from the melt. [c] Total lamellar thickness = POSS + 2PEO + $2PE^{am}$ + PE^{cr}. [d] The overall PE layer thickness = $2PE^{am}$ + PE^{cr}.

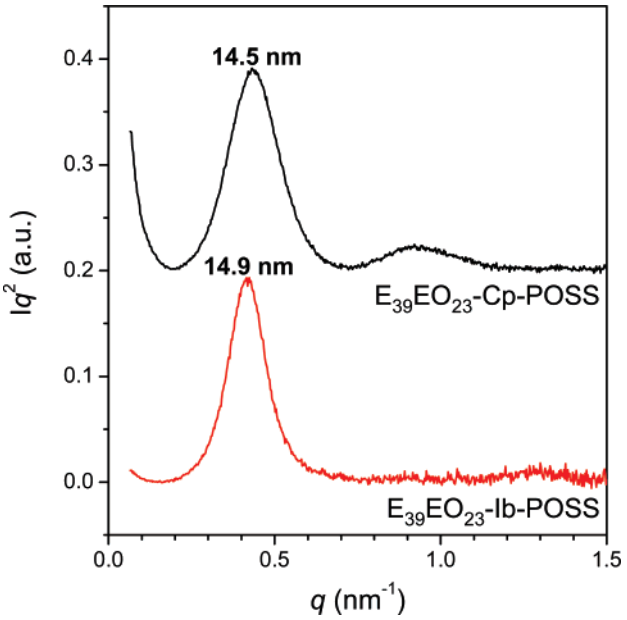

Figure 4. Lorentz-corrected SAXS profiles for $E_{39}EO_{23}$−Cp−POSS and $E_{39}EO_{23}$−Ib−POSS cast from THF solution at ambient temperature.

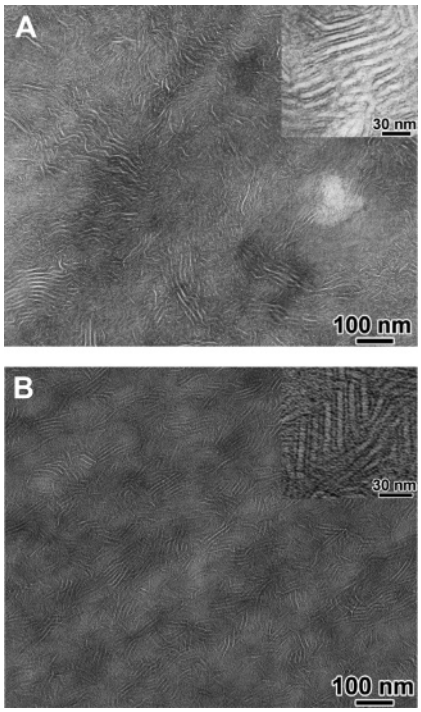

Figure 5. Bright-field TEM micrographs for (A) $E_{39}EO_{23}$−Cp−POSS and (B) $E_{39}EO_{23}$−Ib−POSS cast from THF solutions at ambient temperature. The insets show images under high magnifications. Thin section $E_{39}EO_{23}$−POSS samples were stained by RuO_4 at room temperature for 20 min.

we mentioned above for solution-grown crystals. However, instead of having only straight lamellae with small grains, curved lamellae were also observed. Intriguingly, highly curved lamellar crystals were seen in certain areas, and an example is shown in Figure 8B. Different from genuine onionlike lamellar crystals in a recent report,[41] the centers of these highly curved crystals did not appear to be concentric and the outer lamellae did not form a close loop, possibly due to the high bending rigidity of POSS and PE crystals. Currently, we are still not clear how curvature was induced in the centrosymmetric lamellar structure (i.e., PE−PEO−POSS−PEO−PE layers), even though we speculate that it may relate to unbalanced surface stresses as recently proposed.[41,45] This will need further investigation in the future.

Once-Folded Chain PE Crystals Grown from the Melt in $E_{39}EO_{23}$−Cp−POSS. When $E_{39}EO_{23}$−Cp−POSS is subject to a stepwise heating process, simultaneous SAXS and WAXD profiles are shown in Figure 10. At 25 °C, 2 orders of relatively broad lamellar reflections were seen in the SAXS profile with the *q*-ratio being 1:2. Because the PE crystals were premelted at 110 °C to facilitate sample loading into a thin-wall capillary X-ray tube (diameter = 0.7 mm), the starting lamellar thickness was 13.4 nm instead of 14.5 nm as in the THF-cast samples. We speculate that partial melting and recrystallization of PE crystals might induce fractionally folded chain crystals (this will need further study). This lamellar thickness did not change up to 80 °C, suggesting that fractionally folded PE chains cannot be annealed to thicken in $E_{39}EO_{23}$−Cp−POSS. This is opposite to the lamellar thickening upon heating of the PEO amphiphilic starlike molecules,[17] and we speculate that the incompressibility of POSS molecules prevented PE lamellae from thickening upon heating. When the temperature increased to 85 °C, a small new reflection peak developed at 0.67 nm^{-1} (corresponding to a spacing of 9.35 nm), suggesting the onset of PE crystal melting in the sample. With further increasing the temperature to 100 °C, this new peak became more pronounced and broad lamellar reflection at 0.45 nm^{-1} (*d*-spacing = 13.4 nm) almost disappeared. The PE crystallinity substantially dropped in the WAXD profile at 100 °C. At 105 °C, the PE (110) reflection completely disappeared in the WAXD profile, and in the SAXS profile a relatively sharp reflection peak with a weak second-

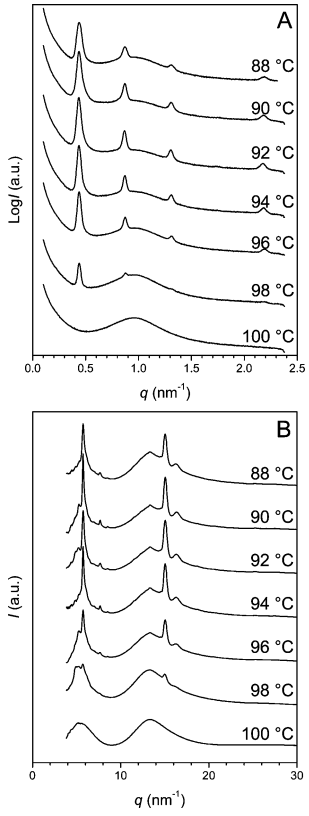

Figure 6. (A) SAXS and (B) WAXD profiles for $E_{39}EO_{23}$−Ib−POSS during a slow heating process from 88 to 100 °C at 1 °C/min.

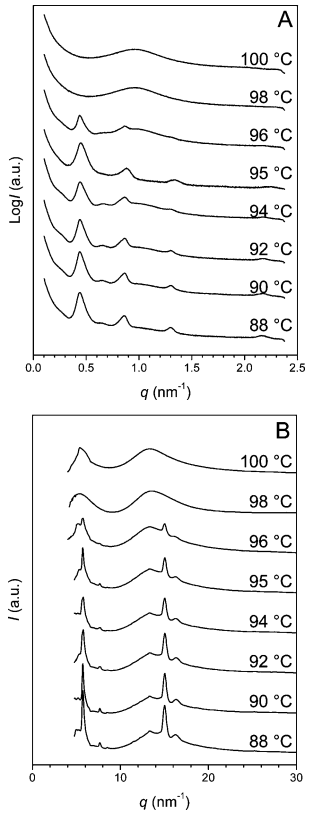

Figure 7. (A) SAXS and (B) WAXD profiles for $E_{39}EO_{23}$−Ib−POSS during a slow cooling process from 100 to 88 °C at 1 °C/min.

order reflection was seen at 0.62 nm^{-1} (corresponding to a *d*-spacing of 10.2 nm). Intriguingly, the POSS ($10\bar{1}1$) reflection did not disappear at 105 °C. Further increasing the temperature to 155 °C, up to 3 orders of sharp lamellar reflections were

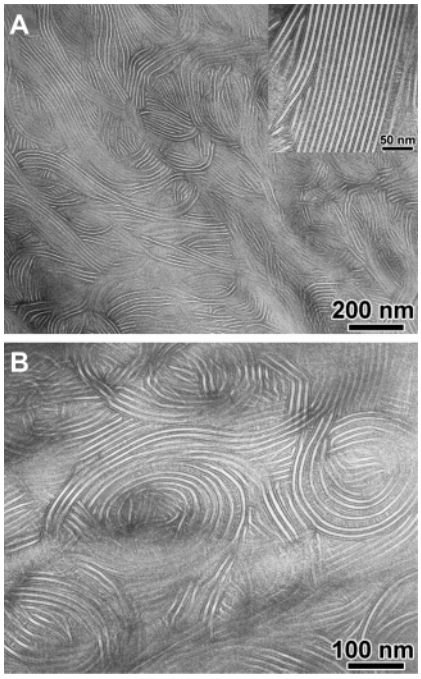

Figure 8. Bright-field TEM micrographs for thin sections of $E_{39}EO_{23}$−Ib−POSS grown from the melt. A low-magnification image is shown in (A), together with a high-magnification image as the inset. Note that both straight (in the inset image) and curved lamellar crystals are observed. Sometimes, highly curved lamellar crystals are also seen as shown in (B). The thin section samples were stained by RuO_4 at room temperature for 20 min.

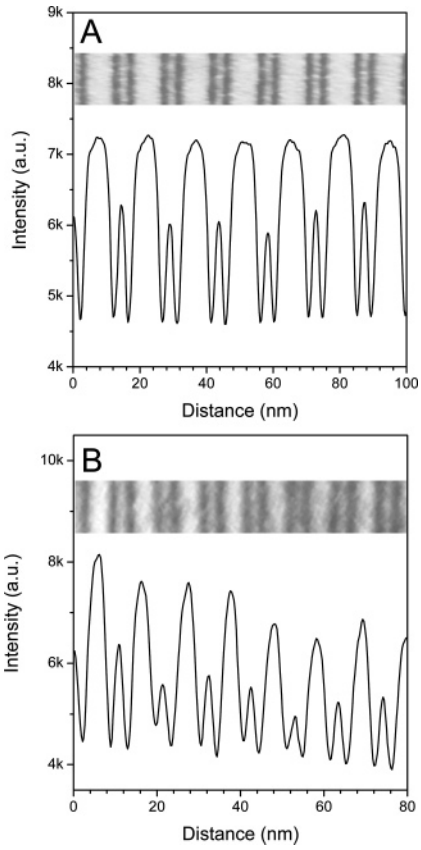

Figure 9. TEM image scan results for (A) $E_{39}EO_{23}$−Ib−POSS and (B) $E_{39}EO_{23}$−Cp−POSS grown from the melt.

seen in the SAXS profile, and the POSS ($10\bar{1}1$) intensity in the WAXD only slightly decreased. The overall lamellar *d*-spacing remained the same at 10.3 nm. Finally, when the temperature

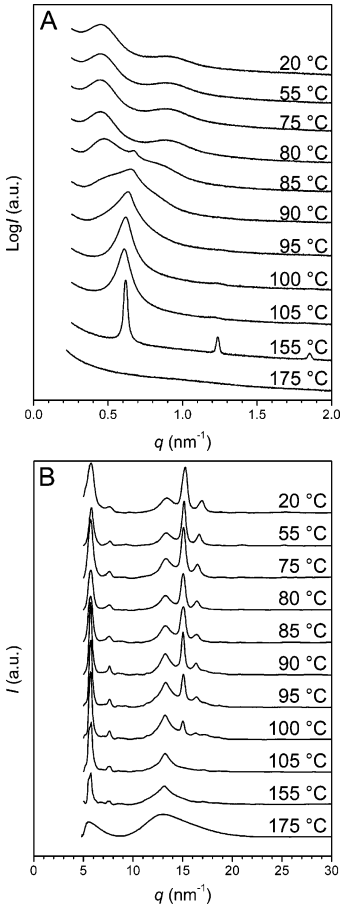

Figure 10. (A) SAXS and (B) WAXD profiles for $E_{39}EO_{23}$−Cp−POSS during a stepwise heating process. The sample was held at each temperature for 5 min before the X-ray measurement.

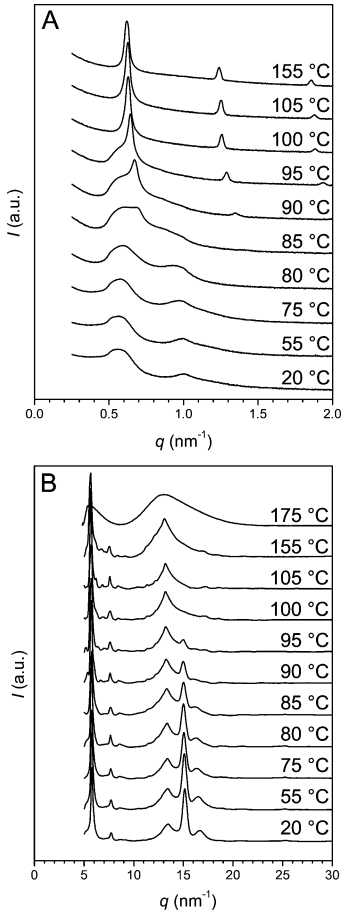

Figure 11. (A) SAXS and (B) WAXD profiles for $E_{39}EO_{23}$−Cp−POSS during a stepwise cooling process from the melt. The sample was held at each temperature for 5 min before the X-ray measurement.

increased to 175 °C, above the melting temperature of 164.1 °C, the sharp lamellar reflections completely disappeared, and a very weak correlation-hole scattering is seen around 1.0 nm^{-1} in the SAXS profile. In the WAXD, two relatively broad amorphous halos were seen, representing the molten state of the sample. This result is consistent with our previous DSC results; after PE crystal melting, the POSS lamellar crystals retained a well-defined lamellar morphology with an overall lamellar thickness of 10.3 nm.

In a stepwise cooling process from the melt at 175 °C, two amorphous halos are seen in the WAXD profile in Figure 11B. The POSS ($10\bar{1}1$) reflection appeared at 155 °C, suggesting the crystallization of POSS blocks. Meanwhile, up to 3 orders of sharp lamellar reflections were observed in SAXS. This lamellar structure remained at an almost constant position until 100 °C. At 95 °C, a broad reflection peak with a larger *d*-spacing started to emerge, and also the PE (110) reflection was seen in the WAXD profile. By decreasing the temperature to 80 °C, the sharp lamellar reflections gradually shifted to higher *q* values and finally disappeared. In the WAXD, the PE (110) reflection became stronger. With further decreasing the temperature to 55 °C, the PE crystallinity reached a maximum and 2 orders of relative broad lamellar reflections were seen in the SAXS. The overall lamellar *d*-spacing was 10.8 nm. Comparing this lamellar thickness with the calculated lamellar thickness having the once-folded chain conformation in Table 1, PE chains were almost once-folded after confined crystallization from the melt (by the POSS lamellar crystals).

Typical TEM images of the melt-grown $E_{39}EO_{23}$−Cp−POSS are shown in Figure 12. Only straight lamellae with relatively large grain sizes (>500 nm) were observed. The inset shows a high-magnification image of straight lamellae. From the TEM image analysis in Figure 9B, we obtained each layer thickness for POSS, PEO, and PE for melt-grown $E_{39}EO_{23}$−Cp−POSS, and the results are also given in Table 1. As we can see, the experimental thicknesses also match reasonably well to the calculated values for the once-folded PE chain conformation. We thus conclude that almost once-folded PE crystals were obtained after confined crystallization from the melt sandwiched between lamellar POSS crystals. Because the ratio between the cross-sectional areas for a PE chain and a POSS molecule in a lamellar crystals with once-folded PE chains decreased to $a_2/2a_1 = 1.3$, surface stresses due to unbalanced interfacial areas were, to a large extent, released, and relatively large grain sizes were obtained for the melt-grown $E_{39}EO_{23}$−Cp−POSS. Com-

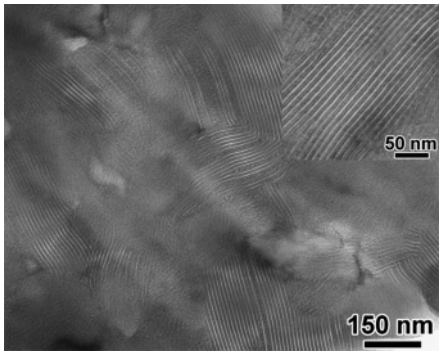

Figure 12. Bright-field TEM micrographs for a thin section of $E_{39}EO_{23}$−Cp−POSS grown from the melt. The thin section sample was stained by RuO_4 at room temperature for 20 min.

paring with the melt-grown $E_{39}EO_{23}$−Ib−POSS having extended PE chain crystals, the nanoconfinement by preexisting lamellar POSS crystals should be responsible for the formation of once-folded PE crystals grown from the melt.

Conclusions

In this work, we successfully attached an oligomeric $E_{39}EO_{23}$-OH diblock copolymer to two kinds of isocyanate POSS molecules, namely, Ib−POSS and Cp−POSS, via the urethane reaction. After stringent purification by column chromatograph, the $E_{39}EO_{23}$−POSS triblock oligomers had a relatively narrow molecular weight distribution around 1.05. Because both ends of the PEO block were tethered to two other blocks, it became noncrystallizable with only a T_g at −59 °C. The self-assembly behavior and PE chain-folding of the $E_{39}EO_{23}$−POSS triblock oligomers were substantially influenced by the unbalanced interfacial areas between a PE chain (cross-sectional area = 0.216 nm^2) and a POSS molecule (cross-sectional area = 1.136 nm^2) in the crystalline lamellae.

First, the PE chains tilted 32° from the lamellar normal, which is ca. 10° higher than the tilt angle of 22° in the neat $E_{39}EO_{23}$ diblock oligomer. We speculate that the higher chain-tilting angle may be a result of the unbalanced interfacial areas between a PE chain and a POSS molecule. POSS molecules crystallized into lamellar crystals with a trigonal $R\bar{3}m$ structure, which was found to be the same as those of neat POSS crystals. The Ib−POSS and Cp−POSS crystal unit cell dimensions were determined to be the same: a = 1.62 nm, c = 1.72 nm, and γ = 120°. Because of the attachment of $E_{39}EO_{23}$ to POSS molecules, only ABCA four-layer lamellar crystals were observed, and crystal twinning was not observed for $E_{39}EO_{23}$−POSS triblock oligomers.

Second, extended-chain PE crystals were observed when the $E_{39}EO_{23}$−POSS samples were cast from THF, which is a good solvent for POSS molecules and a poor solvent for the PE blocks. We speculate that PE crystallization occurred before POSS crystallization during the solvent evaporation process. The unconfined PE crystallization resulted in extended-chain PE crystals. In these extended-chain PE crystals, the interfacial area ratio between a PE chain and a POSS molecule was as high as 2.6 and thus induced small lamellar grain size of ∼100 nm.

Third, when crystallizing from the melt, PE crystallization (or melting) induced almost immediate POSS crystallization (or melting) in the $E_{39}EO_{23}$−Ib−POSS sample. Because of the unconfined PE crystallization, extended-chain PE crystals were obtained. Relatively small grains and curved lamellar crystals were observed in the melt-grown samples due to the imbalance in the interfacial areas between PE and POSS. On the contrary, when crystallizing from the melt in $E_{39}EO_{23}$−Cp−POSS, POSS lamellar crystals formed (at 155.8 °C) before PE crystallization at 96.2 °C. Confined PE crystallization by the existing POSS crystals induced almost once-folded PE crystals. Because the interfacial area ratio reduced to 1.3 for once-folded chain PE crystals, relatively large grains with straight crystalline lamellae (>500 nm) were observed. The dramatic difference in the self-assemblies between $E_{39}EO_{23}$−Ib−POSS and $E_{39}EO_{23}$−Cp−POSS is attributed to the fact that Ib−POSS has a much lower melting point (136.6 °C) than Cp−POSS (357.3 °C).

Acknowledgment. This work was supported by NSF CAREER Award DMR-0348724, DuPont Young Professor Grant, and 3M Nontenured Faculty Award. H.L. thanks the NSF REU program, DMR-0353894. The synchrotron X-ray experiments were carried out at the National Synchrotron Light Source, Brookhaven National Laboratory, supported by the U.S. Department of Energy. Assistance from Dr. Lixia Rong and Prof. Benjamin Hsiao at State University of New York at Stony Brook for synchrotron X-ray experiments is highly acknowledged.

Supporting Information Available: Text giving the synthesis of $E_{39}EO_{23}$−POSS triblock molecules, thermal behaviors of Cp−POSS, Ib−POSS, and $E_{39}EO_{23}$, crystal orientation and crystal structure studied by X-ray diffraction for this paper and figures showing SEC of $E_{39}EO_{23}$, $E_{39}EO_{23}$−Ib−POSS and $E_{39}EO_{23}$−Cp−POSS, ^{1}H NMR of $E_{39}EO_{23}$−Ib−POSS and $E_{39}EO_{23}$−Cp−POSS, DSC of Cp−POSS, Ib−POSS, and $E_{39}EO_{23}$, azimuthal scan results for the 2D WAXD pattern for $E_{39}EO_{23}$−Cp−POSS in Figure 2B, 1D WAXD profiles of Cp−POSS, Ib−POSS, $E_{39}EO_{23}$−Ib−POSS, and $E_{39}EO_{23}$−Cp−POSS, and predicted 2D WAXD pattern and molecular model for shear-oriented $E_{39}EO_{23}$−POSS sample. This material is available free of charge via the Internet at http://pubs.acs.org.

References and Notes

(1) DiMarzio, E. A.; Guttman, C. M.; Hoffman, J. D. *Macromolecules* **1980**, *13*, 1194−1198.
(2) Whitmore, M. D.; Noolandi, J. *Macromolecules* **1988**, *21*, 1482−1496.
(3) Vilgis, T.; Halperin, A. *Macromolecules* **1991**, *24*, 2090−2095.
(4) Douzinas, K. C.; Cohen, R. E.; Halasa, A. F. *Macromolecules* **1991**, *24*, 4457−4459.
(5) Unger, R.; Beyer, D.; Donth, E. *Polymer* **1991**, *32*, 3305−3123.
(6) Rangarajan, P.; Register, R. A.; Fetters, L. J. *Macromolecules* **1993**, *26*, 4640−4645.
(7) Nojima, S.; Yamamoto, S.; Ashida, T. *Polym. J.* **1995**, *27*, 673−682.
(8) Lee, L. B. W.; Register, R. A. *Macromolecules* **2004**, *37*, 7278−7284.
(9) Ashman, P. C.; Booth, C. *Polymer* **1975**, *16*, 889−896.
(10) Booth, C.; Pickles, C. J. *J. Polym. Sci., Polym. Phys. Ed.* **1973**, *11*, 249−264.
(11) Viras, F.; Luo, Y.-Z.; Viras, K.; Mobbs, R. H.; King, T. A.; Booth, C. *Makromol. Chem.* **1988**, *189*, 459−469.
(12) Yang, Y.-W.; Tanodekaew, S.; Mai, S.-M.; Booth, C.; Ryan, A. J.; Bras, W.; Viras, K. *Macromolecules* **1995**, *28*, 6029−6041.
(13) Ryan, A. J.; Fairclough, J. P. A.; Hamley, I. W.; Mai, S.-M.; Booth, C. *Macromolecules* **1997**, *30*, 1723−1727.
(14) Mai, S.-M.; Fairclough, J. P. A.; Viras, K.; Gorry, P. A.; Hamley, I. W.; Ryan, A. J.; Booth, C. *Macromolecules* **1997**, *30*, 8392−8400.
(15) Hong, S.; Yang, L.; MacKnight, W. J.; Gido, S. P. *Macromolecules* **2001**, *34*, 7009−7016.
(16) Opitz, R.; Lambreva, D. M.; de Jeu, W. H. *Macromolecules* **2002**, *35*, 6930−6936.
(17) Miao, J.; Xu, G.; Zhu, L.; Tian, L.; Uhrich, K. E.; Avila-Orta, C. A.; Hsiao, B. S.; Utz, M. *Macromolecules* **2005**, *38*, 7074−7082.
(18) Cui, L.; Miao, J.; Zhu, L.; Sics, I.; Hsiao, B. S. *Macromolecules* **2005**, *38*, 3386−3394.
(19) Huang, X. D.; Goh, S. H. *Macromolecules* **2001**, *34*, 3302−3307.
(20) Kim, B.-S.; Mather, P. T. *Macromolecules* **2002**, *35*, 8378−8384.
(21) Sun, L.; Liu, Y.; Zhu, L.; Hsiao, B. S.; Avila-Orta, C. A. *Polymer* **2004**, *45*, 8181−8193.
(22) Kim, B.-S.; Mather, P. T. *Polymer* **2006**, *47*, 6202−6207.
(23) Kim, B.-S.; Mather, P. T. *Macromolecules* **2006**, *39*, 9253−9260.
(24) Massa, M. V.; Carvalho, J. L.; Dalnoki-Veress, K. *Eur. Phys. J. E* **2003**, *12*, 111−117.
(25) Massa, M. V.; Dalnoki-Veress, K. *Phys. Rev. Lett.* **2004**, *92*, 255509.
(26) Massa, M. V.; Lee, S. M.; Dalnoki-Veress, K. *J. Polym. Sci., Part B: Polym. Phys.* **2005**, *43*, 3438−3443.
(27) Lotz, B.; Kovacs, A. J. *Polym. Prepr. (Am. Chem. Soc., Div. Polym. Chem.)* **1969**, *10* (2), 820−821.
(28) Chen, H.-L.; Hsiao, S. C.; Lin, T. L.; Yamauchi, K.; Hasegawa, H.; Hashimoto, T. *Macromolecules* **2001**, *34*, 671−674.
(29) Chen, H.-L.; Wu, J. C.; Lin, T. L.; Lin, J. S. *Macromolecules* **2001**, *34*, 6936−6944.
(30) Larsson, K. *Ark. Kemi* **1960**, *16*, 203−208.
(31) Larsson, K. *Ark. Kemi* **1960**, *16*, 209−214.
(32) Larsson, K. *Ark. Kemi* **1960**, *16*, 215−219.
(33) Fu, B. X; Hsiao, B. S.; Pagola, S.; Stephens, P.; White, H.; Rafailovich, M.; Sokolov, J.; Mather, P. T.; Jeon, H.; Phillips, S.; Lichtenhan, J.; Schwab, J. *Polymer* **2001**, *42*, 599−611.
(34) Waddon, A. J.; Coughlin, E. B. *Chem. Mater.* **2003**, *15*, 4555−4561.
(35) Zheng, L.; Waddon, A. J.; Farris, R. J.; Coughlin, E. B. *Macromolecules* **2002**, *35*, 2375−2379.
(36) Waddon, A. J.; Zheng, L.; Farris, R. J.; Coughlin, E. B. *Nano Lett.* **2002**, *2*, 1149−1155.

(37) Zheng, L.; Hong, S.; Cardoen, G.; Burgaz, E.; Gido, S. P.; Coughlin, E. B. *Macromolecules* **2004**, *37*, 8606−8611.
(38) Carroll, J. B.; Waddon, A. J.; Nakade, H.; Rotello, V. M. *Macromolecules* **2003**, *36*, 6289−6291.
(39) Cui, L.; Collet, J. P.; Xu, G.; Zhu, L. *Chem. Mater.* **2006**, *18*, 3503−3512.
(40) Zhu, L.; Huang, P.; Chen, W. Y.; Weng, X.; Cheng, S. Z. D.; Ge, Q.; Quirk, R. P.; Senador, T.; Shaw, M. T.; Thomas, E. L.; Lotz, B.; Hsiao, B. S.; Yeh, F.; Liu, L. *Macromolecules* **2003**, *36*, 3180−3188.
(41) Sun, L.; Zhu, L.; Rong, L.; Hsiao, B. S. *Angew. Chem., Int. Ed.* **2006**, *45*, 7373−7376.
(42) Sun, L.; Ginorio, J. E.; Zhu, L.; Sics, I.; Rong, L.; Hsiao, B. S. *Macromolecules* **2006**, *39*, 8203−8206.
(43) Sakamoto, N.; Hashimoto, T. *Macromolecules* **1998**, *31*, 3292−3302.
(44) Sakamoto, N.; Hashimoto, T. *Macromolecules* **1998**, *31*, 3815−3823.
(45) Lotz, B.; Cheng, S. Z. D. *Polymer* **2005**, *46*, 577−610.

MA070770W